Biomaterials 301 (2023) 122273

Contents lists available at ScienceDirect

Biomaterials

journal homepage: www.elsevier.com/locate/biomaterials

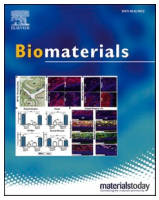

# Brain tissue mechanics is governed by microscale relations of the tissue constituents

P. Sáez [a,b,**], C. Borau [c], N. Antonovaite [d], K. Franze [e,f,g,*]

[a] Laboratori de Càlcul Numèric (LaCàN), Universitat Politècnica de Catalunya, Barcelona, Spain
[b] Institute of Mathematics of UPC-BarcelonaTech (IMTech), Barcelona, Spain
[c] Multiscale in Mechanical and Biological Engineering, Aragon Institute of Engineering Research (I3A), Department of Mechanical Engineering, University of Zaragoza, 50018, Zaragoza, Spain
[d] Department of Physics and Astronomy and LaserLab Amsterdam, Vrije Universiteit Amsterdam, De Boelelaan 1085, 1081 HV, Amsterdam, Netherlands
[e] Department of Physiology, Development, and Neuroscience, University of Cambridge, Downing Street, Cambridge, CB2 3DY, UK
[f] Institute of Medical Physics and Microtissue Engineering, Friedrich-Alexander-Universität Erlangen-Nürnberg, 91052, Erlangen, Germany
[g] Max-Planck-Zentrum für Physik und Medizin, 91054, Erlangen, Germany

ARTICLE INFO

*Keywords:*
Brain mechanics
Mechanobiology
Inmunochemistry
Soft tissue mechanics
Tissue engineering

ABSTRACT

Local mechanical tissue properties are a critical regulator of cell function in the central nervous system (CNS) during development and disorder. However, we still don't fully understand how the mechanical properties of individual tissue constituents, such as cell nuclei or myelin, determine tissue mechanics. Here we developed a model predicting local tissue mechanics, which induces non-affine deformations of the tissue components. Using the mouse hippocampus and cerebellum as model systems, we show that considering individual tissue components alone, as identified by immunohistochemistry, is not sufficient to reproduce the local mechanical properties of CNS tissue. Our results suggest that brain tissue shows a universal response to applied forces that depends not only on the amount and stiffness of the individual tissue constituents but also on the way how they assemble. Our model may unify current incongruences between the mechanics of soft biological tissues and the underlying constituents and facilitate the design of better biomedical materials and engineered tissues. To this end, we provide a freely-available platform to predict local tissue elasticity upon providing immunohistochemistry images and stiffness values for the constituents of the tissue.

## 1. Introduction

Many biological processes in the brain involve mechanical interactions of cells with their surrounding tissue [1]. Cells exert forces on their environment and probe and respond to its local mechanical properties. Accordingly, CNS tissue mechanics is an important regulator of cell function during development [2,3] and disease [4]. During normal ageing and pathological processes, CNS tissue constituents change, including the extracellular matrix (ECM), myelin sheets around neuronal axons, and the number of cells [5–7]. These structural alterations are accompanied by changes in tissue mechanics [8,5].

During the last decades, extensive experimental tests have been performed to determine mechanical properties of the brain (see, among many others, [9–19]). Nowadays, there is a clear consensus that the brain exhibits time-dependent behavior [14,19], both at small and large strains, and that elastic behavior dominates viscoelasticity at the cell and tissue level [20]. The elastic modulus of CNS tissue, a measure of its elastic stiffness, ranges from, approximately, 0.1–2 kPa [11,13,19]. This range of stiffness has been observed across species and different regions of the CNS [16–18]. However, while our knowledge of how brain tissue behaves mechanically at the tissue scale has progressed substantially, how individual brain components contribute to macroscopic brain tissue mechanics is still poorly understood.

Most current mechanical models of brain tissue (see Refs. [19,21]) homogenize the behavior of the tissue constituents into a single constitutive law without further consideration of what components are present or how each of them is organized within specific brain regions [9–11,13,19]. Although there has been a large amount of research devoted to understanding the brain's composition and architecture, this information has so far only sparsely found its way into advanced

* Corresponding author. Institute of Medical Physics and Microtissue Engineering, Friedrich-Alexander-Universität Erlangen-Nürnberg, 91052, Erlangen, Germany.
** Corresponding author. Laboratori de Càlcul Numèric (LaCàN), Universitat Politècnica de Catalunya, Barcelona, Spain.
*E-mail address:* kf284@cam.ac.uk (K. Franze).

https://doi.org/10.1016/j.biomaterials.2023.122273
Received 31 March 2022; Received in revised form 14 June 2023; Accepted 7 August 2023
Available online 10 August 2023

mechanical models of the brain [22–24]. However, like in other biological tissues composed of networks of cells and ECM, the arrangement and stiffness of the underlying brain constituents should determine the mechanics of the organ as a whole.

The definition of a Strain Energy Density Function (SEDF) has been the standard approach in the characterization of soft biological tissues [25]. Within this thermodynamic framework, the contribution of each individual tissue constituent is gathered by an additive decomposition of a SEDF per constituent. Naturally, the additive decomposition of the SEDF imposes affine deformations in the tissue constituents. In other words, it implies that the tissue constituents are arranged in parallel to each other. However, such approach may not accurately reproduce how the tissue components actually assemble.

CNS tissue is mainly built of two cell types, neurons and glial cells. Fig. 1a presents an overview about the main components of the brain and their distribution in the tissue. Pyramidal and granular neurons represent 90% of all neurons in the hippocampus, and the remaining 10% mainly consist of GABAergic interneurons [26]. Some neuronal axons are wrapped by oligodendrocytes, a type of glial cells. The resulting myelin sheath surrounds axons to improve electrical conductivity, and it is characterized by a comparatively high stiffness [27–29]. In addition to oligodendrocytes, other types of glial cells are found in CNS tissue, with astrocytes being the most abundant glial cells in mammals.

The ECM [30] provides adhesion sites for cells to organize into distinct regions. However, unlike in other biological tissues, the ECM of the CNS lacks an abundant collagen network, which is a main determinant of tissue stiffness, and is instead mostly composed of hyaluronic acid (HA) and proteoglycans [31]. Morphologically, the CNS ECM is divided into three main structures that create a scaffold with mechanical and functional roles: perineuronal net (PNNs), the neural interstitial matrix (NIM), and the basal lamina (BL) [32]. The relative ratios of PNNs and NIM components across different brain regions are still not known. In addition to the ECM, blood vessels pass through the tissue.

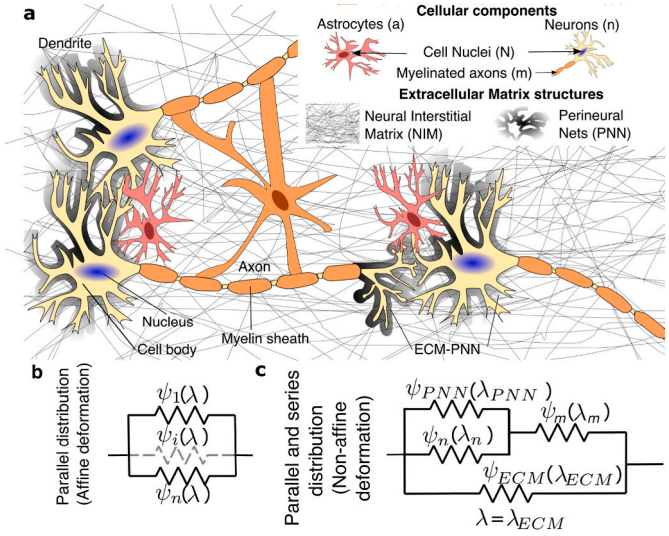


**Fig. 1.** (a) Description of the micro-anatomical structures of the brain. We consider cell bodies, $\rho_n$, perineural nets (PNN, black translucent), $\rho_{PNN}$, myelinated axons (orange), $\rho_m$, and neural interstitial matrix (NIM), $\rho_{NIM}$, which may include blood vessels. PNNs surround neuronal cell bodies and dendrites and the NIM surrounds glial and neuronal cells. We also differentiate between neurons, $\rho_n$ (yellow) and glial cells, $\rho_a$ (pink). (b–c) Distribution of tissue constituents and modeling of a simplified 1D model based on a classical parallel arrangement (b) and on the distribution presented in this work (c): PNNs are linked in parallel with the neuronal somata, which are linked to the myelinated axons in series. These two elements in series are linked with the NIM in parallel. $\psi_i$ is the SEDF of each tissue constituent. $\lambda$ and $\lambda_i$ is the total stretch in the affine scheme (b) and the stretch of each constituent in the non-affine scheme (c), respectively.

Recent studies have started to investigate the relationship between the stiffness of specific brain regions and their constituting structures using phenomenological linear regression models [17,18,23,24]. However, although we already know the mechanical properties of individual neurons and glial cells [20,33–35], and that the presence of myelinated axons has a clear impact on the mechanics of brain tissue [7,15,36], we still do not fully understand how the multiple constituents of CNS tissue ensemble to establish its mechanical behavior at the tissue scale.

The goal of this study was to test the role of the connectivity of individual tissue components in determining local mechanical brain properties at the tissue scale, and to provide a tool to the community that enables the estimation of heterogeneities in local brain tissue stiffness based on immunofluorescence images. Focusing on the hippocampus and cerebellum of the mouse brain, we developed a mechanical model accurately describing tissue-scale brain mechanics, taking into account the mechanical properties of individual brain tissue components and their connectivity.

## 2. Materials and Methods

### 2.1. Sample preparation, ROI identification, indentation protocol and image acquisition

All experimental protocols and data have been previously described and published (see details in Refs. [18,23]). In summary, horizontal brain tissue slices of 300 μm thickness were extracted from 3 to 4 mm of dorsal-ventral positions from two age groups of wild-type mice (C57Bl6/Harlen): juvenile (1 month-old) and young adult (6 and 9-month-old). Each brain tissue slice was placed in a glass bottom chamber for imaging with an inverted microscope, supplied with carbogenated artificial cerebrospinal fluid to maintain the viability and gently pressed down with harp for stabilization. All measurements were performed within 8 h. Up to 12 regions of interest were identified in the hippocampus and three in the cerebellum. For dynamics mechanical experiments, the indentation setup consisted of a cantilever-based ferrule-top probe (0.2–0.5 N/m stiffness and 60–105 μm bead radius) mounted on a piezo transducer and XYZ micromanipulator. Indentation lines were selected to cross the dentate gyrus and the subiculum or the CA3 field of hippocampus (n $\geq$ 66 measurement points per slice). In addition, indentations on cortex were performed on 5 of the same slices adjacent to subiculum, in parallel lines between outer and inner layers (n $\geq$ 21 measurement points per slice). The sample was indented up to 10–17 μm to avoid effects of surface roughness and of sensing individual brain components so that tissue heterogeneities within each region of interest were homogenized. The indentation depth was also chosen to stay in the small strain regime ($\varepsilon_T > 5\%$). Indentation was performed by imposing oscillations of 0.2 μm amplitude and 5.62 Hz frequency on top of the ramp loading at 0.01 strain rate in an indentation-depth controlled mode (see Refs. [18,23] for further results). The raw data was analyzed with an in-house Matlab code to fit the cosine function over oscillatory data to extract storage and loss moduli as a function of indentation-depth:

$$E'(\omega) = \frac{F_0}{h_0} cos(\delta) \frac{\sqrt{\pi}(1-\nu^2)}{2\sqrt{A}} \quad (1)$$

$$E''(\omega) = \frac{F_0}{h_0} sin(\delta) \frac{\sqrt{\pi}(1-\nu^2)}{2\sqrt{A}} \quad (2)$$

where $F_0$ and $h_0$ are the amplitudes of oscillatory load and indentation-depth, respectively, $\delta$ is the phase-shift between indentation and load oscillations, $\nu$ is the Poisson's ratio (assumed to be 0.5 as brain tissue is a nearly incompressible material) and $A$ is the contact area. Indentation mapping was performed at 50 μm step size over regions in hippocampus and cerebellum for tissue slices from juvenile brain (N = 6) and only over hippocampus for adult brain slices (N = 5). Each indentation location was assigned to the measured ROI. The Hertz model was used to

fit the initial loading data to obtain the precise the contact point location which is needed for the estimation of contact radius. We also compared our small strain approximation to the large strain theory by performing finite element simulation in Abaqus (see SI for details).

### 2.2. Image adquisition and analysis

Images of immunohistochemically stained slices were previously obtained and used here for further analysis [23]. In short, two age groups of 3 wild-type mice (C57Bl6/J) were used to stain nuclei of neurons (NeuN), all cell nuclei (Hoechst), astrocytes (GFAP), myelin (MBP) and dendrites (MAP2). Details on the antibodies used for the (immuno)histochemical staining are provided elsewhere [23]. Fluorescence images were obtained with a Zeiss Axioscope.A1 epi-microscope with a 10x Plan-NeoFluar objective. Anatomical regions were identified and drawn manually as polygons using ImageJ and their coordinates stored in.roi files.

We analyzed image data using custom-written MATLAB codes which allowed automatic processing of multiple images by providing their corresponding ROIs coordinates. To minimize intensity disparity due to acquisition conditions, we preprocessed all images to adjust their histograms to match the histogram of an arbitrarily chosen reference image. After that, every color channel was individually normalized by its maximum intensity value. Subsequently, for every pixel of each image, the percentage of each color channel intensity ($p_r$, $p_g$, $p_b$) was computed. Then, for each ROI and each channel (c) we calculated the weighted mean ($\widehat{p}_{w,c}^{ROI}$) of the color intensity percentage, using the total intensity of each pixel (the sum of the three channel intensities) as weight:

$$\widehat{p}_{w,c}^{ROI} = \left(\sum_{n=1}^{N_{pix}^{ROI}} p_c^n \cdot i_{tot}^n\right) \Big/ \left(\sum_{n=1}^{N_{pix}^{ROI}} i_{tot}^n\right) \tag{3}$$

Multiplying the weighted mean intensity of each channel by the total average intensity of the ROI ($i_{av}^{ROI}$) is equivalent to calculating the average channel intensity ($i_{c,av}^{ROI}$), which is later used to weight the storage and loss modulus of each of the brain components (see Supp. Material).

$$\widehat{p}_{w,c}^{ROI} \cdot i_{av}^{ROI} = i_{c,av}^{ROI} \tag{4}$$

### 2.3. Homogenization method

Here, we followed a mean-field (MF) homogenization scheme to describe the mechanical behavior of the tissue (see SI for details). Microstructure heterogeneities are treated separately as homogeneous phases, and the quantities of interest in the microstructure are just averaged values for the macroscopic response. We define our Representative Volume Element (RVE) such that it contains a large number of microstructural features and, therefore, has a statistical representation of the macroscopic material [37]. In our problem, we can define a length at the microstructures that correspond to somas (10um), axons (1-2μm in diameter), and the components of the EMC. We assumed that our RVE, which was on the order of 50um, was large enough compared with the microscopic length scales. Note, that we were limited by the size of some ROIs in the hippocampus, which were as small as 50 μm.

Based on these assumptions, we describe two basic models. One in which the tissue constituents are all assembled in parallel and the other in which they are in series. We describe here the homogenization scheme in a small strain setting, which recovers the Voigt and Reuss estimates, respectively [38,39]. The derivation from the large strain setting is described in the SI.

We first describe the model with all the tissue constituents arranged in parallel (see Fig. 1b). The total Cauchy stress tensor is given as

$$\boldsymbol{\sigma}_T = \sum_i^n \rho_i \boldsymbol{\sigma}_i, \tag{5}$$

where the stress-strain constitutive relation for each constituent is defined as

$$\boldsymbol{\sigma}_i = \mathbb{C}_i : \boldsymbol{\epsilon} \tag{6}$$

$\boldsymbol{\epsilon}$ is the infinitesimal strain tensor, or Cauchy's strain tensor, defined as $\boldsymbol{\epsilon} = \frac{1}{2}\left[\nabla \mathbf{u} + (\nabla \mathbf{u})^{\mathrm{T}}\right]$, where $\mathbf{u}$ is the displacement tensor. Note that, we assumed that the strain in each constituent is the same as the macroscopic strain tensor. $\mathbb{C}_i$ is the fourth-order stiffness tensor of each constituent *i*. The constitutive law of the tissue is therefore uniquely determined by the stiffness tensor, which, assuming the tissue to be isotropic and almost incompressible, is a function of the storage modulus E (a measure of tissue stiffness). Finally, we can combine Eqs. (5) and (6) and write $\boldsymbol{\sigma}_T = \sum_i^n \rho_i \mathbb{C}_i : \boldsymbol{\epsilon}$. Considering the indentation tests, we can write the final stress-strain relation

$$\sigma_T = E_T \epsilon, \quad \text{where} \quad E_T = \sum_i^n \rho_i E_i \tag{7}$$

is the total equivalent elastic modulus obtained from the indentation tests, that is the total stiffness of the tissue due to the presence of several constituents with elastic moduli $E_i$.

If we consider brain tissue constituents arranged in series, stress will be now constant along the elements and strains will vary. To generalize this idea within a consistent thermodynamic formulation, we took advantage of the complementary energy density function (cSEF) (see Refs. [40–42] and SI). The additive decomposition of the cSEDF naturally imposes non-affine deformations in the tissue constituents, which resembles the classical Reuss estimate [39].

In the linear regime, we can express the total infinitesimal strain tensor as

$$\boldsymbol{\epsilon}_T = \sum \rho_i \boldsymbol{\epsilon}_i, \tag{8}$$

where the stress-strain constitutive relation for each constituent is defined as

$$\boldsymbol{\epsilon}_i = \widehat{\mathbb{C}}_i : \boldsymbol{\sigma}. \tag{9}$$

$\widehat{\mathbb{C}}_i$ is the compliance tensor of each tissue constituent, which, again, is a function of E and the Poisson's ratio. Combining the two previous equations, we obtain $\boldsymbol{\epsilon}_T = \sum_i^n \rho_i \widehat{\mathbb{C}}_i : \boldsymbol{\sigma}$. Considering the indentation tests, we can write the final stress-strain relation as

$$\sigma = E_T \epsilon_T, \quad \text{where} \quad E_T = \frac{\prod_i^n \rho_i E_i}{\sum_i^n \rho_i E_i} \tag{10}$$

is the total equivalent elastic modulus obtained from the indentation tests.

### 2.4. Fitting of material parameters

We used a custom-written MATLAB code to fit the storage and loss moduli, E' and E", for each constituent. We made use of the *fmincon* function to find the minimum of a constrained nonlinear multivariable goal function,

$$Error = \sqrt{\Sigma_{i=1}^n \left(E_i - E_i^e\right)_i^2 \Big/ n - q} \Big/ \mu_{p_i} \tag{11}$$

here $n$ is the number of ROIs, $i$ represents each ROI and $\mu_{p_i}$ denote the mean of the experimentally measured E′ and E". In addition, $q$ is the number of parameters of the model, such that $n - q$ denotes the number of degrees of freedom.

## 3. Results

### 3.1. Local hippocampus composition correlates with tissue stiffness

First, we analyzed the local composition of the juvenile mouse hippocampus, using immunohistochemistry. We focused on myelin (using myelin binding protein, MBP, as marker), as an indicator of myelinated axons [7], nuclei of neurons (NeuN), nuclei of all cells (Hoechst), and astrocytes (glial fibrillary acidic protein, GFAP) in different regions of interest (ROIs) of the tissue (Fig. 2a–e and SI Appendix, Fig. S14)), as reported elsewhere [23]. Large variations in densities of the individual markers over the different ROIs where observed [23] (Fig. 2f and Table S1).

The granular cell layer (GCL), which mainly consists of neuronal cell bodies, reached the highest concentration of nuclei with ~ 46%, while the amount of myelin was just a residual 0.5%, the lowest of all ROIs (see Materials and Methods). The Alveus (Alv), on the other hand, which is a region containing mainly myelinated fibers that cover the ventricular parts of the hippocampus, had the highest concentration of myelin, ~ 50%, while the amount of cell nuclei reached 15%. All other regions presented a more uniform distribution of tissue components, in agreement with previous image analysis results [23] (for details see Fig. 2f–k and Table S1).

In order to quantify the fraction of neuronal and glial cell nuclei, the distributions of NeuN and the astrocyte marker GFAP were measured [18,23]. ROIs with higher amounts of cell nuclei (GCL, Sub and SP3, Fig. 2f) had the largest ratio of neuronal nuclei to total number of nuclei (see Fig. 2k) and showed a low concentration of GFAP (Fig. 2 and Table S1). Other regions, including the ML, SR1, SR3, SLM, Hilus and Alveus, were characterized by a low ratio of neuronal/total cell numbers and a high concentration of GFAP, confirming previous descriptions of the spatial heterogeneity of brain tissue components in the hippocampus [6].

To account for the remaining, non-cellular components of the tissue, we made the following assumption for the fraction of ECM and, in particular, of PNNs and NIM: $\rho_{ECM} = 1 - (\rho_N + \rho_m)$, that is, the space not occupied by either nuclei ($\rho_N$) or myelin ($\rho_m$) is assumed to be ECM. Then, we assume that NIM is more prevalent in regions where more astrocytes ($\rho_a$) are present and PNNs where more neuronal nuclei ($\rho_n$) are localized. The stiffness of smaller blood vessels with diameters comparable to those of other tissue components is effectively included in the stiffness of the NIM. Therefore, we defined $\rho_{NIM} = \rho_{ECM}{}^{*}\rho_a/(\rho_n + \rho_a)$ and $\rho_{PNN} = \rho_{ECM}{}^{*}\rho_n/(\rho_n + \rho_a)$ (SI Appendix, Figs. S1–3).

Then, we compared recently published data of the stiffness of each ROI (see Materials and Methods and [23] for further details) with the distribution of each ROI's components. Tissue stiffness had been measured using a nanoindentation approach, where forces were applied that were similar in magnitude and time scale as the forces exerted by CNS cells [2,43]. Means and standard deviations of the storage moduli E′, which are a measure of the tissue's elastic component, for each ROI at every indentation level, $\delta$, are provided in Fig. S6. We focused on an applied $\delta = 13$ μm (Fig. 2,l-m), but all the features described next were consistent along the different $\delta$(SI Appendix, Fig. S10, Tables S12–13).

In summary, the lowest value of E' ~ 0.3 kPa was obtained for the GCL. As shown in Fig. 2, the GCL is a region mostly occupied by neuronal cells, specifically granular cells and astrocytes, with a comparatively small number of myelinated axons (5%). The SP3, which mostly consists of pyramidal neurons and a moderate amount of myelinated axons

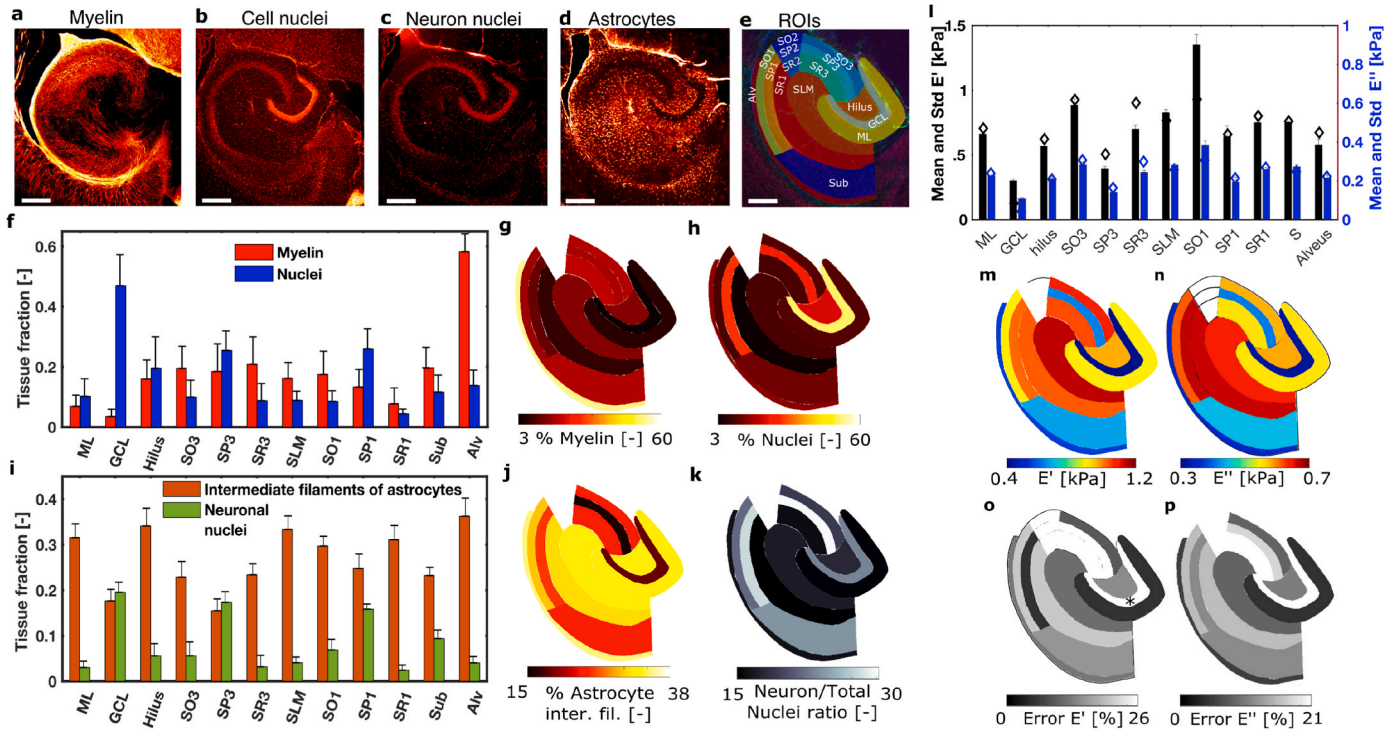


**Fig. 2.** Imaging and quantification of brain tissue composition and stiffness values of juvenile mice. Imaging of (a) myelin (MBP), (b) cell nuclei (Hoechst), (c) nuclei of neurons (NeuN) and (d) intermediate filaments of astrocytes (GFAP) in specific regions of the hippocampus. (e) Abbreviations used for regions are: Alv - alveus, Sub - subiculum, SLM - stratum lacunosum moleculare, SR - stratum radiatum, SP - stratum pyramidale, SO - stratum oriens, ML - molecular layer, GCL - granule cell layer. White regions indicate excluded due to similarity with adjacent regions. Scale bars (a–e) are 200 μm. Mean and standard deviation of the tissue components quantification (f–k). Mean and standard deviation of the myelin and nuclei (f) and representation of the mean value in each specific ROI (g–h). Mean and standard deviation of the neuron nuclei and intermediate filament of filaments of astrocytes (i) and representation of the mean value of intermedia filaments and the ratio between neuron vs. total nuclei in each specific ROI (j–k). (l) Mean and standard deviation of E′ and E″ for the different regions of the hippocampus. Diamond marks shows the prediction of the proposed mechanical model and bars show the measured values. (m–n) Representation of E′ and E″ in all the ROIs. (o–p) Error of the proposed mechanical model for E′ and E″ represented in each ROI.

(20%), was the second softest region (~0.4 kPa). These two regions were characterized by the highest fraction of neuronal nuclei in the hippocampus. Surprisingly, the third softest region was the Alveus (~0.7 kPa), a region containing almost 60% of myelinated axons, few neuronal cell bodies, and a substantial number of astrocytes. Most other ROIs fell in the 0.8–1.2 kPa range. The stiffest ROIs was the SO1, with E' ~ 1.3 kPa, which has a moderate fraction of astrocytes (30%) and low amounts of other stained components.

To analyze how the tissue composition regulates tissue rigidity, we first investigated the correlation between the tissue fractions (Fig. 2) and the stiffness of all ROIs (SI Appendix, Fig. S4 and Table S2). We observed negative correlations between structure and stiffness for all tissue constituents except for the fraction of astrocytes, which showed a positive correlation. Only the correlations between tissue stiffness and the densities of all nuclei and those of neurons alone had a significant Pearson's correlation coefficient ($r = -0.69$ and $r = -0.66$, respectively), in agreement with previous data [23]. These results indicated that the characteristic mechanical signature of each ROI may be related to the local tissue composition, and that tissue mechanics likely results from a combination of all the constituents rather than being dominated by one single component.

### 3.2. Brain mechanics cannot be explained through affine deformation of its components

To test this hypothesis, we set out to define a constitutive law describing the stiffness of each ROI by incorporating information about the local tissue composition. Previous work correlating stiffness and tissue composition in the nervous system developed phenomenological models assuming linear and non-linear relationships to reproduce composition-stiffness relations [22,23] or assuming that only the tissue component with the highest correlation with the tissue stiffness contributes to its rigidity [24]. Here, we derived a homogenized model, based on a mean-field (MF) approach, to predict brain tissue mechanics as a function of the distribution and stiffness of each tissue constituent. The representative volume of material is defined such that it contains a large number of microstructural features. In our problem, the length of individual brain components is on the order of a few $\mu$m (nuclei, <10 μm; axons, 1–2 μm; ECM filaments, 10 nm). The representative volume of our analysis was chosen to be 50 μm × 50 μm in x and y, respectively, as a compromise between the small dimensions of the mouse hippocampus and the size of microstructural features (see Materials and Methods, point 2.1 for further details. We first defined a MF model based on the total SEDF $\Psi_T$ of the system, the density energy required to deform the tissue under an external load (we provide a complete derivation in the SI Appendix). This is a standard approach in modeling soft biological tissues (e.g. arteries [25,44], cartilage [45] and brain tissue [21]). Within the small strain limit, and assuming that the tissue is isotropic, almost-incompressible, and that bonds between constituents are strong so that slippage does not occur at small strains [46], we can define the stress-strain relations as a function of the storage modulus E (a measure of tissue stiffness). The total equivalent $E_T$ of the tissue, that is the total stiffness of the tissue due to the presence of several constituents with elastic modulus $E_i$ and fraction $\rho_i$, is $E_T = \sum_i^n \rho_i E_i$, which recovers the classical Voigt estimation [38] (see Section 2.3 and SI).

Following the additive decomposition of the SEDF, we took the values of tissue composition quantification (Fig. 2) and performed a fitting procedure against the experimental values of $E'$ at different indentation levels (see Materials and Methods). We fixed the storage modulus of cell nuclei to $E'_N = 0.6$ kPa and took the modulus of myelinated axons, $E'_m = 2.0$ kPa, and of the PNN and NIM, $E'_{PNN} = 1$ kPa and $E'_{NIM} = 1$ kPa, respectively, as initial seeds of the fitting procedure, in agreement with previously published values [5,20,33,35,47]. The fitting procedure yielded mean errors in all regions and indentation levels of ~21% based on the fraction of their components (SI Appendix Fig. S10 and Tables S12–13). $E'_m$ increased linearly from ~0.3 kPa at $\delta = 6.5$ μm up to ~1.3 kPa at $\delta = 17$ μm, and $E'_{PNN}$ and $E'_{NIM}$ also increased linearly from ~0.5 kPa and 0.2 kPa up to 1.7 kPa and 0.7 kPa, respectively.

As mentioned above, the additive decomposition of the SEDF imposes a parallel arrangement of the brain constituents and, therefore, an affine deformation of the tissue constituents. In such affine deformations, the stiffest component dominates the mechanical response of the tissue. The stiffest component of the brain, according to literature, are myelinated axons, with elastic moduli between ~2 kPa-1MPa [20,48]. However, the fitted E' values for myelin (~0.2–0.6 kPa, SI Appendix, Fig. S12) were lower than these published values. Even if we consider the lowest range of the myelinated axons, stiffness values of 2–20 kPa, and impose it into the additive decomposition of the SEDF, it would lead to an equivalent stiffness of the tissue of ~3–12 kPa (the component stiffness multiplied by its tissue fraction). This resulting stiffness of the tissue represents errors of ~300–1500%, 1–2 orders of magnitude higher than the errors found when the model parameters were freely fitted by the minimization algorithm, suggesting that affine deformations cannot explain the observed behaviour. Moreover, it can be argued that tissue components are not all connected in parallel. Neurons have clearly differentiated regions (e.g. cell bodies and the myelinated axons) with specific mechanical properties [20], which must deform in a non-affine manner under an imposed force.

These findings and arguments suggest that the mechanical response of the brain could not follow an additive decomposition of the SEDF or, equivalently, be explained through affine deformations of its constituents.

### 3.3. Non-affine deformations of brain components explain tissue mechanics

To evaluate possible explanations of the inconsistencies described above, and to derive a physical model capable of solving them and predicting local tissue stiffness based on the mechanical properties and arrangements of its constituents, we took a closer look at the brain tissue structure (Fig. 1). Some of the tissue constituents do not assemble in the tissue in a parallel arrangement but rather in series, as for example myelinated axons and their somata. Thus, the modeling limitations described for the additive decomposition of the SEDF could arise from the inherent affine deformation imposed on the tissue constituents. If tissue constituents arrange in series, forces are transmitted continuously in all the elements and the constituents will be subjected to non-affine deformations. We can generalize this idea within a consistent thermodynamic formulation, taking advantage of the complementary energy density function (cSEDF), $\widehat{\Psi}$ [41,42]. In terms of the reduced storage modulus, the equivalent $E'_T$ of $n$ components arranged in series, i.e. defined through its cSEDF, is $E'_T = \prod_i^n E'_i / \sum_i^n E'_i$, which recovers the Reuss estimate [39] (see Section 2.3 and SI). We particularize this approach to our problem and model the structural organization as follows (see Fig. 1c): PNNs are linked in parallel with the neuronal somata, which are linked to the myelinated axons in series. These two elements in series, on the other hand, are linked with the NIM in parallel. We also assumed that the adhesion between cells and their environment is strong at the tested time and length scales. Therefore,

$$E'_T = \frac{(\rho_n E'_n + \rho_{PNN} E'_{PNN}) * \rho_a E'_a}{\rho_n E'_n + \rho_{PNN} E'_{PNN} + \rho_a E'_a} + \rho_{NIM} E'_{NIM}. \quad (12)$$

We then used this structural description of the tissue to analyze whether we could reproduce the mechanical properties of the tissue applying Eq. (12). We took again $E'_N = 0.4$ kPa and $E'_m = 2.0$ kPa as an initial seed for the fitting procedure [20,33,35,47], assumed that the PNNs have the same stiffness as the NIM, and fitted all values of $E'_i$ for each constituent. The fraction, $\rho_i$, was again obtained from the tissue quantification

(Fig. 2). We focused on an indentation of $\delta = 13$ μm (other indentation levels are shown in SI Appendix, Figs. S6–8 and Tables S5–8).

Our theoretical model predicted the experimentally measured mechanical response of all locations in all ROIs with a mean error below 19% (see Fig. 3g,h and SI Appendix, Tables S5–6), showing a slight improvement with respect to the affine model (21%). Most regions showed remarkably low errors below 15% except for the GCL (64%), SP3 (26%), SR3 (26%) and SR1 (23%) regions. Note that we obtained these low errors with a clear and physical meaning of the main tissue constituents analyzed in this study. In Table S9, we present the results of E′ for each indentation depth analyzed. The NIM and PNN showed a slightly non-linear strain-stiffening behavior. Considering only one type of ECM resulted in higher errors, which suggests that PNN and NIM could have different stiffness values. The PNN stiffness increased linearly from ~3 kPa, at $\delta = 6.5$ μm, up to ~8.5 kPa at $\delta = 17$ μm and the NIM stiffness increased linearly from ~0.5 kPa up to 1.5 kPa. Myelin showed a linear increase in the stiffness with increasing $\delta$ as well (see Fig. S8), from 2 kPa up to 7.5 kPa. E' values reported in Table S9 are consistent with directly measured stiffness values of neurons, myelin and ECM [5,20,33,35,47], which was not achieved in the affine model. Values of the NIM are also consistent with the stiffness of substrates on which neurons and glial cells differentiate [49,50].

### 3.4. Viscoelasticity depends on tissue architecture

To investigate whether the additive decomposition of the cSEDF could be used for analyzing not only tissue elasticity but also the viscoelastic behavior of the brain [12,14], we applied our model to a frequency-dependent characterization of the tissue. We took the loss moduli E″, which represent the viscous component of the mechanical response, of each ROI (see Materials and Methods) and plotted the mean values and standard deviation in Fig. 3g. Then, we applied the relation as in Eq. (12) but for the loss modulus E" to describe the viscoelastic response of each ROI based on its local composition, and performed the same fitting procedure as above (see Table S9). As shown in Fig. 3g,h, we found a good agreement between experimental data and the theoretical model, with a mean error lower than 16%, and most of the ROIs with errors lower than 15% except, again, the GCL, SP3, and SR3 regions, which slightly overpassed this threshold. The reported loss moduli for all components were again comparable to data from literature [20,33,35,47] and showed similar increases with increasing indentation depths (SI Appendix, Table S9).

### 3.5. Composition and stiffness of brain components reproduce CNS mechanics

To further investigate the general applicability of our model, we extended our study to the hippocampus of adult mice by using previously reported data [18]. The tissue composition in the adult hippocampus is shown in Fig. 3 and SI Appendix, Table S1. We focused again on $\delta = 13$ μm (other indentation depths are shown in SI Appendix, Fig. S5 and Tables S3-4,S9). We observed a stiffening of both the ECM (PNN and NIM) and cell bodies compared to the juvenile samples, which is in line with previously published data on rodent brain tissue stiffening during development and ageing [3,5]. We found a same tendency for the loss modulus E" (see Fig. 3 and SI Appendix, Table S9).

Using our model (Eq. (12)), we were able to reproduce the mechanical properties of the adult hippocampus with an average error of measurements of 25% and 27% for E′ and E″, respectively. Again, these values represent a decrease with respect to the errors obtained with the affine model, 31% and 35% for E' and E", respectively. The hilus and SP3 were the only regions with error higher than 40%. It is important to note, however, that the model accurately captured the tendency of the age-related change in tissue rigidity for all ROIs. Moreover, the stiffness values found by the fitting procedure were again within the values reported in literature [20,33,35,47], which was not possible for the affine model. The myelin and NIM stiffness showed a linear increase with increasing indentation depths. However, the myelin stiffness showed a slight decrease with respect to the juvenile samples while the stiffness of the NIM doubled its values with respect to the juvenile animals. The PNN was again the stiffest component of the brain.

Finally, we applied our model to a different region of the brain, the cerebellum of juvenile mice, by using previously reported data [23] (Fig. 4). We predicted E′ and E″ of different ROIs (see Fig. 4) considering the distribution of the cerebellum's components (Fig. 4d-i) and the fitted values of E′ obtained for the components of the juvenile hippocampus (Fig. 3 and Table S9). The model was able to reproduce the cerebellum's heterogenous mechanics [23] (Fig. 4k–j) without any further fitting of parameters and they were again within the values reported in literature [51].

We found mean errors of 21% and 15% for E′ and E″, respectively, which were lower than the 23% and 41% for E' and E", respectively,

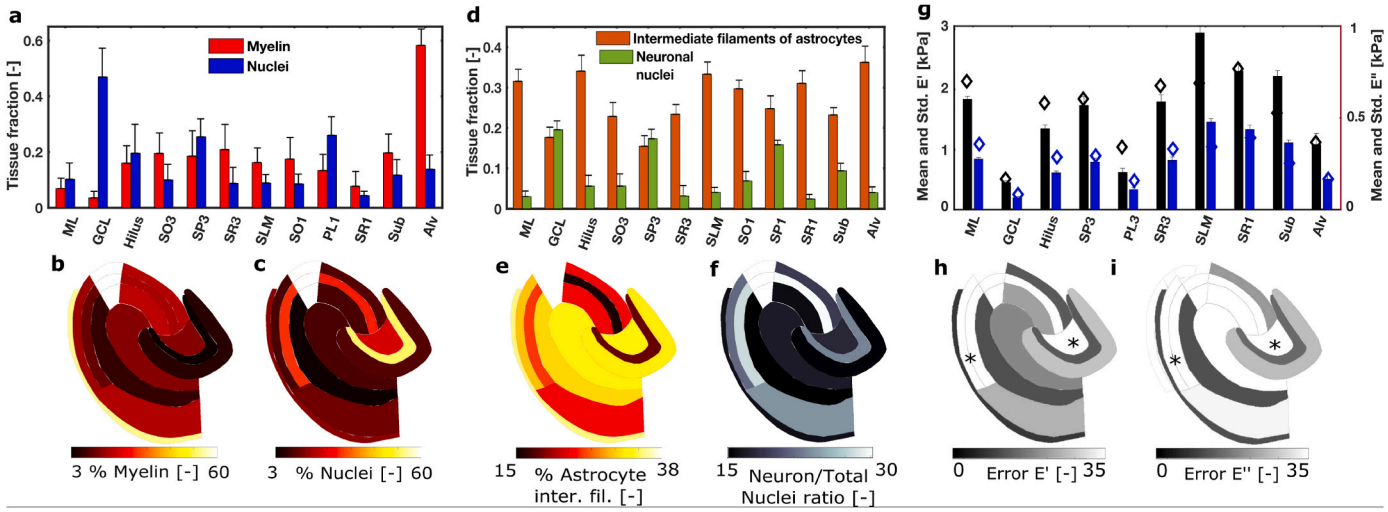


**Fig. 3.** Quantification and analysis of tissue composition and stiffness of ROIs for the hippocampus of juvenile mouse. Mean and standard deviation of the mylein and nuclei (a) and representation of the mean value in each specific ROI (b–c). Mean and standard deviation of the neuron nuclei and intermediate filament of filaments of astrocytes (d) and representation of the mean value of intermedia filaments and the neuron vs. total nuclei in each specific ROI (e–f). Mean and standard deviation of E′ and E″ for the different region of the hippocampus and prediction (diamond marks) of the proposed mechanical model (g). Error of the proposed mechanical model for E′ and E″ represented in each ROI (h–i).

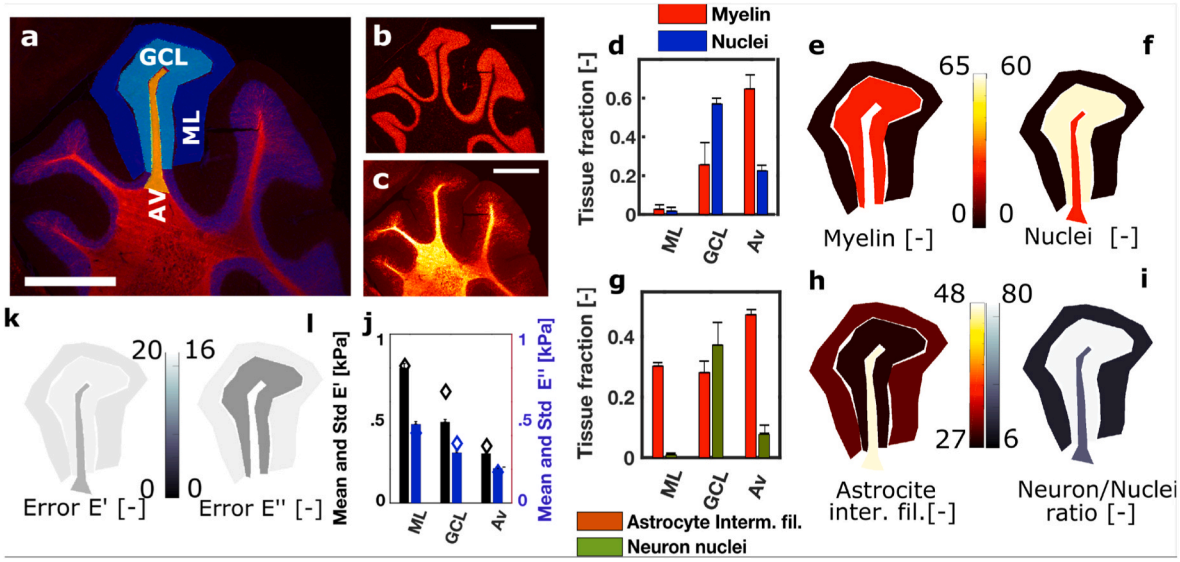


**Fig. 4.** Quantification and analysis of tissue composition and stiffness of ROIs for the cerebellum of juvenile mice (a–c). Nuclei and myelin are shown in blue and red, respectively (a), nuclei (b) and myelin (c). Scale bars (a–e) are 100 μm. Abbreviations used for regions are: GCL = granular cell layer, ML = molecular layer, Av = Arbor vitae. Mean and standard deviation of tissue brain composition (d–i): Mean and standard deviation of the myelin and nuclei (d) and representation of the mean value in each ROI (e–f). Mean and standard deviation of the neuron nuclei and intermediate filaments of astrocytes (g) and representation of the mean value of filaments and the neuron vs. total nuclei ratio in each specific ROI (h–i). Error of the proposed mechanical model for E′ and E″ represented in each ROI (k–l). Mean and standard deviation of E′ and E″ for the different region of the cerebellum (j). Diamond marks shows the prediction of the proposed mechanical model.

yielded by the affine model (see also SI Appendix, Fig. S11 and Tables S14–15). In summary, our results indicated that the non-affine model predicts local nervous tissue mechanics well, irrespective of age and regions, solely based on the distribution and mechanical properties of its constituents, and it outperforms the affine model.

## 4. Discussion

In this study, we developed a mathematical model that uses the morphological structure of brain tissue to determine its local mechanical properties. We found that a classical additive decomposition of the Strain Energy Density Function (SEDF), and equivalently stresses, of each tissue constituent, cannot fully reproduce the complex mechanical behavior of brain tissue. However, when we took the actual structural organization of the tissue into account, we were able to predict brain mechanics. By considering the abundancy and mechanical properties of individual cellular and extracellular tissue components, as well as their arrangement within brain tissue, some being connected in parallel and others in series, we were able to reproduce the local mechanical behavior of the tissue. Finally, we also present an online platform for the scientific community (uploaded in the MATLAB Central File Exchange) that, upon providing immunohistochemistry images and stiffness values for the constituents of the sample, yields the viscoelastic properties at the tissue scale.

Previously developed models (see Refs. [19,21] for a review) often considered a homogenized response of the tissue constituents to applied forces. Other models have considered different tissue components but not their actual properties, proposing constitutive laws that included parameters with unclear physical interpretation [22,23] or have focused on one tissue component with stronger correlation with tissue stiffness [24]. Our results suggest that the classical additive decomposition of the SEDF is not appropriate to reproduce tissue stiffness from the structure and stiffness of its components. We argue that this is due to an inherent affine deformation of such models. By incorporating a precise multi-scale description of the tissue, our model now enables us to predict mechanical properties of specific brain tissue regions, which are characterized by distinct compositions and arrangements of cells and ECM.

We followed a bottom-up approach: based on what we knew about the brain tissue constituents, we reproduced local brain tissue mechanics with minimal fitting parameters. Specifically, we only fitted the storage and loss moduli of myelinated axons, perineuronal nets and interstitial matrix. Ideally, this information could be obtained from separate experiments. Here, we fitted their values and made sure they are within the range of data reported in the literature. Furthermore, we used the fitted values of the storage and loss moduli from the juvenile hippocampus (Table S9) and reproduced, without any further fitting procedure, the stiffness of the juvenile cerebellum (Fig. 4).

We found that, in juvenile samples, the stiffness of the ECM increases non-linearly with increasing strain, that the stiffness of cell bodies does not change with strain, and that the stiffness of myelin increases with strain. In adult tissue, however, the stiffness to tissue constituents changes variably with changing strain levels. Regions with a high concentration of neurons, such as the GCL or the SP3, were reproduced less well than others. Overall, these errors may be attributed to the simplifications used to reconstruct the tissue architecture from 2D immunohistochemistry images, instead of 3D information. The forces applied on structures just below the visualized layer of the tissue may contribute somewhat to the measured mechanical properties of the tissue. We hypothesize that heterogeneities between structures below the plane imaged may also contribute to the slight deviation of our model from the data.

Our results suggest that there are simple mechanical relationships between tissue constituents that regulate the mechanical properties of brain tissue. Incorporating tissue architecture into models describing tissue mechanics could potentially be used for the constitutive modeling of other soft biological tissues, for example, cardiovascular tissue [25,44].

While our model fits the experimental data well, there are still limitations. We used indentation data acquired at small strains and built an elastic and linear model. At large strains, however, brain tissue behaves as a non-linear material and can also show non-elastic responses [19,21]. Extending our current model and experimental tests to a large strain setting will provide further insights into how brain tissue behaves mechanically. Moreover, a detailed analysis of the tissue's anisotropy will be required at large strains. Our model relies on a simple mean-field homogenization method that takes into consideration the 2D

immunohistochemistry data we used for our analysis. A 3D morphological reconstruction of the representative volumes of interest at high resolution would foster more advanced homogenization methods (see, e.g., Refs. [52,53]). This would provide, for example, information on the anisotropy of the tissue. However, we have previously shown that, at small strains and in CNS tissue, structural anisotropy only leads to (a slight) mechanical anisotropy in white matter tissue, where large, myelinated axon bundles are aligned in parallel, but not in grey matter tissue [22], which is structurally much more similar to the tissue modeled in our current study. For other brain regions and strain regimes, the effect of the morphological anisotropy of the tissue should be incorporated.

Finally, our work specifically focuses on how different tissue constituents are organized in parallel and in series, which induces affine and non-affine deformations, respectively. However, previous non-affine models and data of soft tissues rich in collagen suggested that the non-affine regime appears at large strains [54,55]. Other materials, such as polyacrylamide gels, show non-affine deformation at small strains while affine deformation is present at large strains depending on the cross-linking of the network [56]. Although our model is consistent with non-affine deformation even at small strains, our approach can also be applied in a large strain setting [42], and future work will be required to evaluate how different strain levels and load states influence the deformation affinity.

In terms of tissue composition, we have considered all extracellular tissue components homogenized into one single material. But the role of each of these tissue components should be further investigated. For example, how do the different ECM structures contribute to tissue mechanics? What role does the vasculature and the anisotropy play in regulating brain tissue mechanics? We also used a viscoelastic model to focus on the arrangement of the tissue constituents. More advanced viscoelastic models could reproduce the behavior of the tissue even more accurately (see, e.g., Ref. [57]). Separating the role of viscoelasticity from poroelasticity should also be the focus of research for a complete understanding of brain mechanics. Once these data are available, computationally more expensive multiscale finite element methods or advanced mean-field approaches can be applied to investigate brain mechanics with even higher accuracy.

There are still important questions to be answered to improve our current understanding of brain tissue mechanics: for example, do neuronal cells and ECM change their mechanical properties during development? How do cell-ECM interactions and adhesive interfaces change during development and ageing? A precise description of how tissue constituents arrange in soft biological tissue will allow us not only to better understand its mechanical properties but also to design better biomedical materials [58] and engineered tissues [59]. The cooperation of mathematical models, computational bioengineering, image analysis and neuroscience will eventually allow us to answer these and many more questions.

## Credit author statement

P.S designed the work, performed the mechanical simulations. C.B. performed the image analysis. N.A. analyzed the mechanical tests. P.S. and K.F. wrote the paper. All authors analyzed the data and critically reviewed the paper.

## Declaration of competing interest

The authors declare that they have no known competing financial interests or personal relationships that could have appeared to influence the work reported in this paper.

## Data availability

Data will be made available on request.

## Acknowledgements

P.S has been supported by the Generalitat de Catalunya under grants 2017-SGR-1278. N.A acknowledges funding from the European Research Council (Consolidator award 615170). K.F. acknowledges funding from the European Research Council (Consolidator Award 772426), the Alexander von Humboldt Foundation for his Alexander von Humboldt Professorship, and the German Research Foundation (DFG; project 460333672 CRC1540 EBM).

## Appendix A. Supplementary data

Supplementary data to this article can be found online at https://doi.org/10.1016/j.biomaterials.2023.122273.

## References

[1] W.J. Tyler, The mechanobiology of brain functio, Nat. Rev. Neurosci. 13 (12) (2012) 867–878.
[2] D.E. Koser, et al., Mechanosensing is critical for axon growth in the developing brain, Nat. Neurosci. 19 (12) (2016) 1592–1598.
[3] A.J. Thompson, et al., Rapid changes in tissue mechanics regulate cell behaviour in the developing embryonic brain, Elife 8 (2019) 1–18.
[4] P. Moshayedi, et al., The relationship between glial cell mechanosensitivity and foreign body reactions in the central nervous system, Biomaterials 35 (13) (2014) 3919–3925.
[5] M. Segel, et al., Niche stiffness underlies the ageing of central nervous system progenitor cells, Nature 573 (7772) (2019) 130–134.
[6] B.S. Elkin, A. Ilankovan, B. Morrison, Age-dependent regional mechanical properties of the rat hippocampus and cortex, J. Biomech. Eng. 132 (1) (2010), 011010.
[7] J. Weickenmeier, R. de Rooij, S. Budday, T.C. Ovaert, E. Kuhl, The mechanical importance of myelination in the central nervous system, J. Mech. Behav. Biomed. Mater. 76 (2017) 119–124.
[8] K. Franze, P.A. Janmey, J. Guck, Mechanics in neuronal development and repair, Annu. Rev. Biomed. Eng. 15 (1) (2013) 227–251.
[9] F. Pervin, W.W. Chen, Dynamic mechanical response of bovine gray matter and white matter brain tissues under compression, J. Biomech. 42 (6) (2009) 731–735.
[10] J.A.W. van Dommelen, et al., Mechanical properties of brain tissue by indentation: interregional variation, J. Mech. Behav. Biomed. Mater. 3 (2) (2010) 158–166.
[11] T. Kaster, I. Sack, A. Samani, Measurement of the hyperelastic properties of ex vivo brain tissue slices, J. Biomech. 44 (6) (2011) 1158–1163.
[12] S. Budday, et al., Mechanical characterization of human brain tissue, Acta Biomater. 48 (2017) 319–340.
[13] V. Balbi, A. Trotta, M. Destrade, A. Ní Annaidh, Poynting effect of brain matter in torsion, Soft Matter 15 (25) (2019) 5147–5153.
[14] T.P. Prevost, A. Balakrishnan, S. Suresh, S. Socrate, Biomechanics of brain tissue, Acta Biomater. 7 (1) (2011) 83–95.
[15] C. Giordano, S. Kleiven, Connecting fractional anisotropy from medical images with mechanical anisotropy of a hyperviscoelastic fibre-reinforced constitutive model for brain tissue, J. R. Soc. Interface 11 (91) (2014).
[16] N. Bouchonville, et al., AFM mapping of the elastic properties of brain tissue reveals kPa $\mu$m-1 gradients of rigidity, Soft Matter 12 (29) (2016) 6232–6239.
[17] E. Moeendarbary, et al., The soft mechanical signature of glial scars in the central nervous system, Nat. Commun. 8 (2017) 1–11.
[18] N. Antonovaite, S.V. Beekmans, E.M. Hol, W.J. Wadman, Regional variations in stiffness in live mouse brain tissue determined by depth-controlled indentation mapping, Sci. Rep. 8 (12517) (2018) 1–11.
[19] S. Budday, et al., Fifty shades of brain: a review on the mechanical testing and modeling of brain tissue, Arch. Comput. Methods Eng. 27 (2019) 1187–1230, 2020.
[20] Y.B. Lu, et al., Viscoelastic properties of individual glial cells and neurons in the CNS, Proc. Natl. Acad. Sci. U.S.A. 103 (47) (2006) 17759–17764.
[21] A. Goriely, et al., Mechanics of the brain: perspectives, challenges, and opportunities, Biomech. Model. Mechanobiol. 14 (5) (2015) 931–965.
[22] D.E. Koser, E. Moeendarbary, J. Hanne, S. Kuerten, K. Franze, CNS cell distribution and axon orientation determine local spinal cord mechanical properties, Biophys. J. 108 (9) (2015) 2137–2147.
[23] N. Antonovaite, L.A. Hulshof, E.M. Hol, W.J. Wadman, D. Iannuzzi, Viscoelastic mapping of mouse brain tissue: relation to structure and age, J. Mech. Behav. Biomed. Mater. 113 (2021), 104159.
[24] S. Budday, et al., Towards microstructure-informed material models for human brain tissue, Acta Biomater. 104 (2020) 53–65.
[25] J.D. Humphrey, Continuum biomechanics of soft biological tissues, Proc. R. Soc. A: Math. Phys. Eng. Sci. 459 (2029) (2003) 3–46.
[26] S. Campbell, G. MacQueen, The Role of the hippocampus in the Pathophysiology of Major Depression, 2004.
[27] R. Bernal, P.A. Pullarkat, F. Melo, Mechanical properties of axons, Phys. Rev. Lett. 99 (1) (2007), 018301.

[28] A. Heredia, C.C. Bui, U. Suter, P. Young, T.E. Schäffer, AFM combines functional and morphological analysis of peripheral myelinated and demyelinated nerve fibers, Neuroimage 37 (4) (2007) 1218–1226.
[29] W.C. Huang, J.D. Liao, C.C.K. Lin, M.S. Ju, Depth-sensing nano-indentation on a myelinated axon at various stages, Nanotechnology 22 (27) (2011), 275101.
[30] L.W. Lau, R. Cua, M.B. Keough, S. Haylock-Jacobs, V.W. Yong, Pathophysiology of the brain extracellular matrix: a new target for remyelination, Nat. Rev. Neurosci. 14 (10) (2013) 722–729.
[31] S. Dauth, et al., Extracellular matrix protein expression is brain region dependent, J. Comp. Neurol. 524 (7) (2016) 1309–1336.
[32] J.W. Fawcett, T. Oohashi, T. Pizzorusso, The roles of perineuronal nets and the perinodal extracellular matrix in neuronal function, Nat. Rev. Neurosci. 20 (8) (2019) 451–465.
[33] Y.A. Ayala, et al., Rheological properties of cells measured by optical tweezers, BMC Biophys. 9 (1) (2016) 1–11.
[34] K. Pogoda, P.A. Janmey, Glial tissue mechanics and mechanosensing by glial cells, Front. Cell. Neurosci. 12 (February) (2018) 1–9.
[35] E. Spedden, J.D. White, E.N. Naumova, D.L. Kaplan, C. Staii, Elasticity maps of living neurons measured by combined fluorescence and atomic force microscopy, Biophys. J. 103 (5) (2012) 868–877.
[36] Y. Feng, R.J. Okamoto, R. Namani, G.M. Genin, P.V. Bayly, Measurements of mechanical anisotropy in brain tissue and implications for transversely isotropic material models of white matter, J. Mech. Behav. Biomed. Mater. 23 (2013) 117–132.
[37] R. Hill, The elastic behaviour of a crystalline aggregate, Proc. Phys. Soc. 65 (5) (1952) 349–354.
[38] W. Voigt, Ueber die Beziehung zwischen den beiden Elasticitätsconstanten isotroper Körper, Ann. Phys. 274 (12) (1889) 573–587.
[39] A. Reuss, Berechnung der Fließgrenze von Mischkristallen auf Grund der Plastizitätsbedingung für Einkristalle, ZAMM Z. fur Angew. Math. Mech. 9 (1) (1929) 49–58.
[40] R.W. Ogden, Inequalities associated with the inversion of elastic stress-deformation relations and their implications, Math. Proc. Camb. Phil. Soc. 81 (2) (1977) 313–324.
[41] D.J. Reynolds, J.A. Blume, Incompressibility and materials with complementary strain-energy density, J. Elasticity 33 (1) (1993) 89–105.
[42] P. Saez, S.J. Eppell, R. Ballarini, J.F.R. Matas, A complementary energy approach accommodates scale differences in soft tissues, J. Mech. Phys. Solid. 138 (2020), 103895.
[43] Bollmann, et al., Microglia mechanics: immune activation alters traction forces and durotaxis, Front. Cell. Neurosci. 9 (2015) 363.
[44] G.A. Holzapfel, R.W. Ogden, Constitutive modelling of arteries, Proc. R. Soc. A: Math. Phys. Eng. Sci. 466 (2118) (2010) 1551–1597.
[45] V.C. Mow, M.H. Holmes, W. Michael Lai, Fluid transport and mechanical properties of articular cartilage: a review, J. Biomech. 17 (5) (1984) 377–394.
[46] M.A. Garcia, J.B. Zuchero, Anchors away: glia-neuron adhesion regulates myelin targeting and growth, Dev. Cell 16;51 (6) (2019) 659–661.
[47] T. Grevesse, B.E. Dabiri, K.K. Parker, S. Gabriele, Opposite rheological properties of neuronal microcompartments predict axonal vulnerability in brain injury, Sci. Rep. 5 (March) (2015).
[48] R. Bernal, P.A. Pullarkat, F. Melo, Mechanical properties of axons, Phys. Rev. Lett. 99 (1) (2007).
[49] A.J. Engler, S. Sen, H.L. Sweeney, D.E. Discher, Matrix elasticity directs stem cell lineage specification, Cell 126 (4) (2006) 677–689.
[50] A. Banerjee, et al., The influence of hydrogel modulus on the proliferation and differentiation of encapsulated neural stem cells, Biomaterials 30 (27) (2009) 4695–4699.
[51] A.F. Christ, et al., Mechanical difference between white and gray matter in the rat cerebellum measured by scanning force microscopy, J. Biomech. 43 (15) (2010) 2986–2992.
[52] M.G.D. Geers, V.G. Kouznetsova, K. Matouš, J. Yvonnet, Homogenization Methods and Multiscale Modeling: Nonlinear Problems, 2017, pp. 1–34.
[53] P. Kanouté, D.P. Boso, J.L. Chaboche, B.A. Schrefler, Multiscale methods for composites: a review, Arch. Comput. Methods Eng. 16 (1) (2009) 31–75.
[54] J.M. Huyghe, C.J.M. Jongeneelen, 3D non-affine finite strains measured in isolated bovine annulus fibrosus tissue samples, Biomech. Model. Mechanobiol. 1 (11) (2012) 161–170.
[55] P.L. Chandran, V.H. Barocas, Affine versus non-affine fibril kinematics in collagen networks: theoretical studies of network behavior, J. Biomech. Eng. 2 (128) (2005) 259–270.
[56] Q. Wen, A. Basu, P.A. Janmey, A.G. Yodhb, Non-affine deformations in polymer hydrogels, Soft Mater. 8 (2012) 8039–8049.
[57] R. de Rooij, E. Kuhl, Constitutive modeling of brain tissue: current perspectives, Appl. Mech. Rev. 68 (c) (2015) 1–33.
[58] L.L. Hench, J.M. Polak, Third-generation biomedical materials, Science 295 (5557) (2002) 1014–1017.
[59] E. Axpe, G. Orive, K. Franze, E.A. Appel, Towards brain-tissue-like biomaterials, Nat. Commun. 11 (1) (2020) 3423.